Facile One-Pot Synthesis of White Emitting Gold Nanocluster solutions composed of Red, Green and Blue Emitters

Laureen Moreaud,[a] Janak Prasad,[a] Serges Mazères,[b] Cécile Marcelot,[a] Clothilde

Comby-Zerbino,[c] Rodolphe Antoine,[c] Olivier Heintz[d] and Erik Dujardin*[a,d]

[a]   CEMES, CNRS UPR 8011– Université Toulouse III P. Sabatier, 29 rue J. Marvig, 31055 Toulouse, France.
[b]   IPBS, CNRS UMR 5089 – Université Toulouse III P. Sabatier, 205 route de Narbonne, 31077 Toulouse, France.
[c]   ILM, CNRS UMR 5306 - Université C. Bernard Lyon 1, 69100 Villeurbanne, France.
[d]   ICB, CNRS UMR 6303 – Université de Bourgogne Franche-Comté, 9 rue A. Savary, 21078 Dijon, France

*   Corresponding author: erik.dujardin@cnrs.fr

Electronic Supporting Information

Table of contents

1 - Control experiments on the fluorescence emission

Pure EG is crucial in the formation of bright emitting AuNCs. A slight dilution of EG with water leads to an immediate reduction of the mixture fluorescence, irrespective of the excitation energy, until it completely disappears and only larger plasmonic non fluorescent gold nanoparticles are obtained instead of fluorescent AuNCs (Figs. S1a-c). In standard fluorescence spectroscopy experiments, the presence of larger gold nanoparticles is revealed by the second harmonic peak of the excitation corresponding to the diffusion of the excitation light by the metallic surface. These peaks are the only ones present in fluorescence spectra from 10 nm gold nanoparticles stabilized with citrate (Fig S1d), are clearly observed in 95% EG solutions (Fig S1b) or in the absence of EG (Fig S1b) but are not seen in spectra of 100% EG samples (Fig S1a).

The observed fluorescence could be produced by the adducts of other reagents used in our protocol. We have therefore conducted several control experiments by following the same protocol in 100% EG as the generic synthesis but omitting one component. When the aniline is not added, no fluorescence signal is obtained (Fig. S1e). Indole and aniline derivatives are known for their fluorescence. In the absence of gold precursor ($HAuCl_4$) but all other parameters being kept identical, a small emission peak centered at 340 nm is indeed recorded (Fig. S1f for $AuNC_a$ and Fig S1g for $AuNC_i$ protocols) that is absent of all AuNC fluorescence spectra. The origin of this fluorescence was not further investigated.
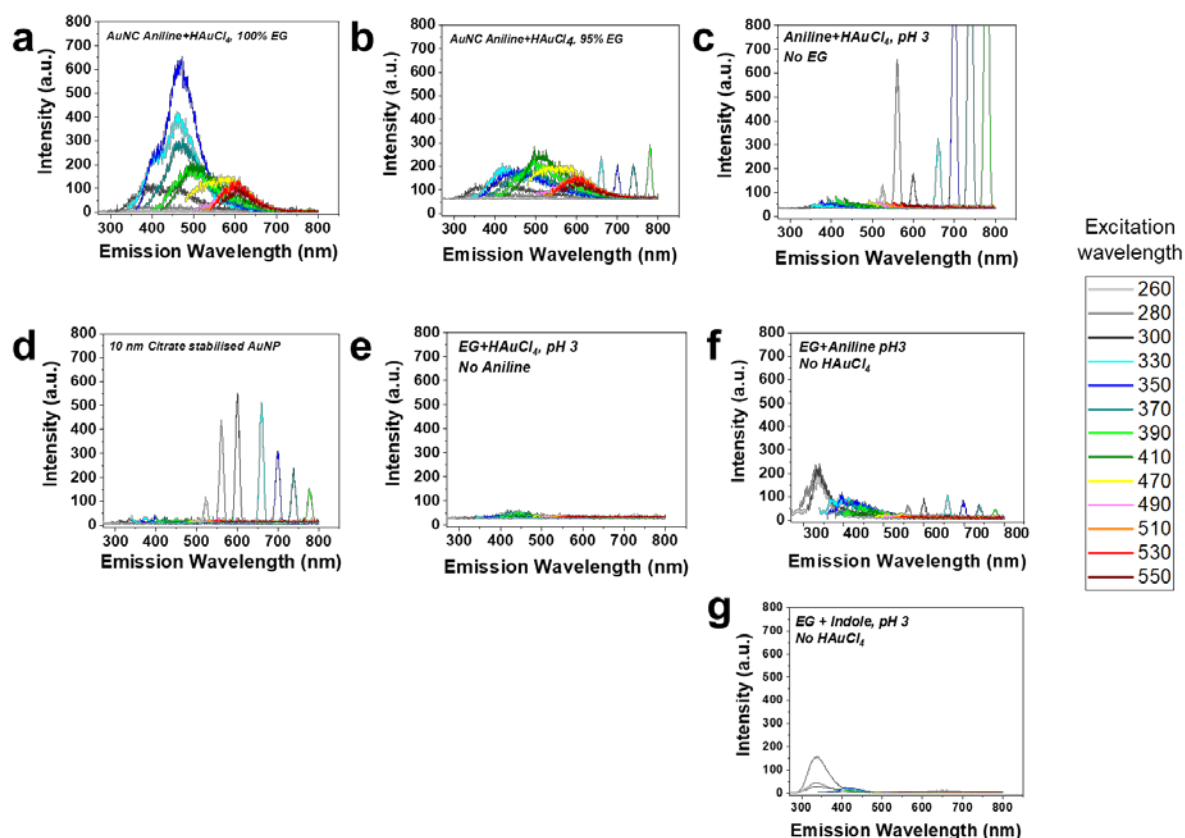
Figure S1: Fluorescence spectra of (a) as-synthetized AuNCs obtained by the standard aniline protocol; (b) a solution produced in 95% EG; (c) a solution produced in the absence of EG. (d) Fluorescence spectra of a solution of 10 nm citrate stabilized AuNPs that exhibit only excitation harmonic scattering. (e,f) Fluorescence spectra of control solutions obtained by the generic protocol without adding (e) aniline or (f) HAuCl4. All panels follow the same color coding of the excitation wavelength shown on the right.

2 - UV-visible absorption spectrum

The UV-vis absorbance spectra of as-synthetized as well as functionalized and dialyzed samples produced with aniline or indole are shown in Figure S2. The decrease of absorbance after the functionalization is attributed to the dilution during the dialysis step.

The peaks with a spectral broadening of the absorption spectrum due to a molecule-like HOMO-LUMO transition is characteristic of ultra-small metallic particles. Only the as-synthesized indole-based solution (Fig. S2b, black curve) shows a peak that could indicate the presence of small plasmonics particles larger than 3 nm diameter. Even though centrifugation of the as-synthetized suspensions reduces the presence of large nanoparticles, EG is viscous and complicates the full removal of the plasmonics colloids. In contrast, the spectra after functionalization and dialysis (red curves) do not show any plasmon peak, indicating that the particles are smaller than 3 nm. The transfer protocol into water described in Experimental Section thus leads to Au nanoclusters solutions free of plasmonic nanocrystals.
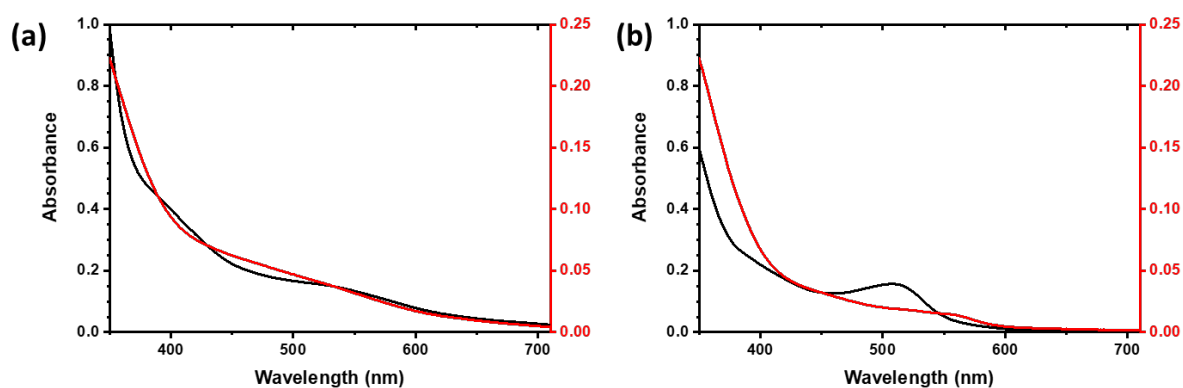
Figure S2. UV-vis absorption spectrum after centrifugation of as-synthetized solution (in black) and functionalized then dialyzed solution (in red) of: (a) aniline-reduced sample and (b) indole-reduced sample.

3. Repeatability of the one-pot AuNC synthesis

The 2D fluorescence maps of several repeats of our one-step synthesis yield highly reproducible positions of the high-intensity areas for both aniline (AuNCa) and indole (AuNCi) protocols even before any post-synthetic processing (centrifugation, dialysis or functionalization).

Figure S3 shows two pairs of 2D fluorescence maps corresponding to two different batches (a,c and b,d) for both protocols, AuNCa (a,b) and AuNCi (c, d). The same excitation / emission areas (pinpointed by sets of black crosses placed at the same coordinates for both batches) are observed with very minor relative intensity changes.

Note that the instrumental noise is higher on the second batch (Figs. S3b, d) due to a lower intensity of the solution emission. In these low concentration conditions, artifacts due to the Raman peaks of the water are visible. Their spectral position varies linearly with the excitation wavelength and so are visible on the 2D map as diagonal straight lines. These artifacts are often used to calibrate fluorescence spectrometers. The presence of water in the second synthesis can be explained by the hygroscopic character of EG. In this particular synthesis, EG with measurable traces of absorbed water was used.
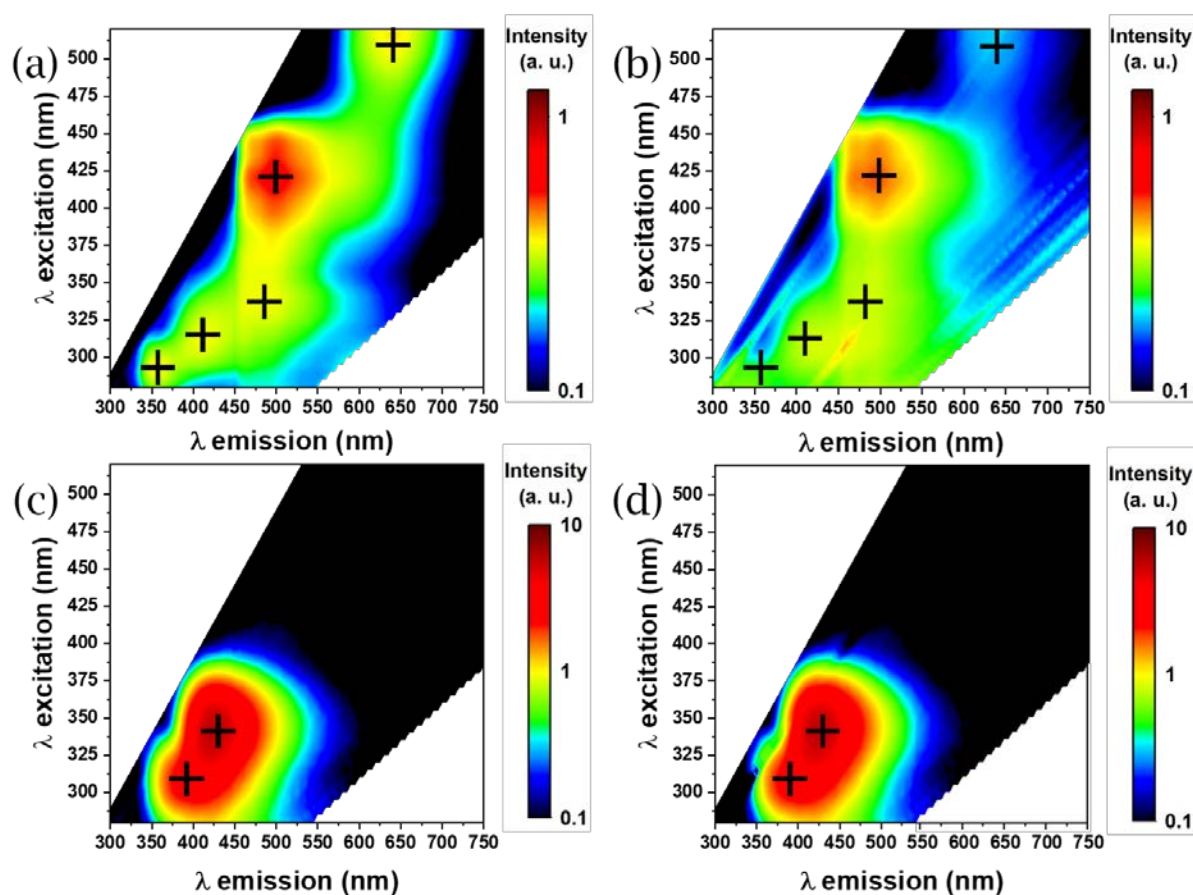
Figure S3 Representative 2D maps of room temperature fluorescence intensity of (a-b) AuNCa and (c-d) AuNCi clusters as a function of emission (λ_{em}) and excitation (λ_{ex}) wavelengths from two different batches. Black crosses in (a) and (b), respectively (c) and (d), are placed at the same (λ_{em}, λ_{ex}) coordinates. The white areas of the 2D plots contain no data, as fluorescence is recorded from 10 nm above λ_{ex} to 10 nm before the second harmonic, $2\lambda_{ex}$.

4. Effect of thiopegylation on photophysical properties

The functionalization of the clusters by water-soluble thiopegylated ligands bearing any of the three considered terminal groups only marginally impacts the spectral positions of the fluorescence features. Figure S4 gathers the 2D fluorescence maps of AuNCa (a,c,e) and AuNCi (b, d, f) after functionalization with (a,b) short PEG amine **1**, (c, d) short PEG carboxylate **2** and (e, f) long PEG biotin **4**. The black cross markers in Fig. S4 are placed in the same (λ_{em}, λ_{ex}) coordinates as in figure S3. In all cases, the luminescence patterns coincide with those of as-synthesized AuNC, irrespective of the ligand. One can note the further blue shift from λ_{em} = 352 nm to λ_{em} = 310-330 nm of the violet emitters in thiopegylated AuNCa.
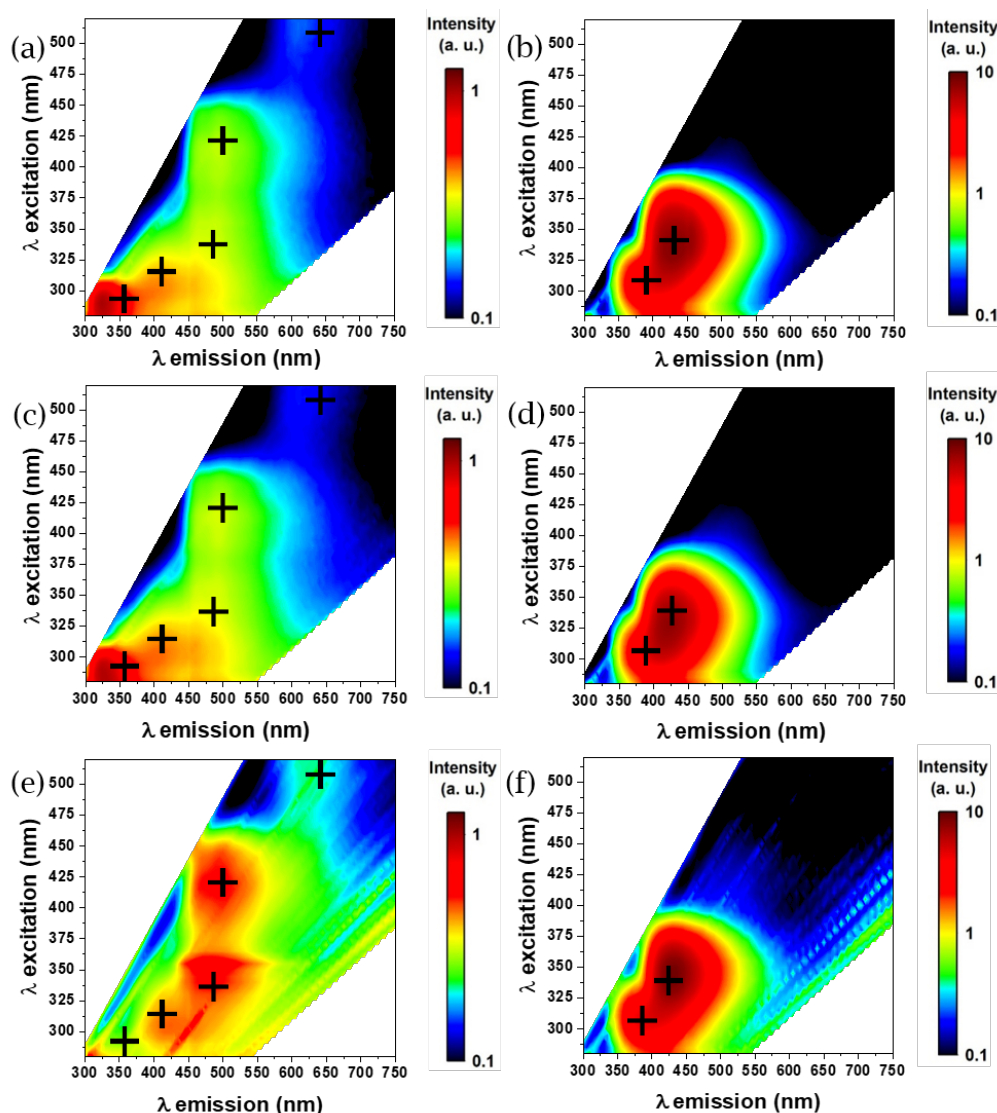
Figure S4: 2D maps of room temperature fluorescence intensity of thiopegylated AuNC (a) 1a, (b) 1i, (c) 2a, (d) 2i, (e) 4a and (f) 4i in water as a function of emission (λ_{em}) and excitation (λ_{ex}) wavelengths.

However, the main impact of the functionalization is a redistribution of the relative intensity between the different emitters for the aniline AuNCa capped with short (PEG$_{12}$) ligands 1a (Fig. S4a) and 2a (Fig. S4c). The strongest emission is no longer the green one (λ_{ex} = 425 nm; λ_{em} = 500 nm) but violet (λ_{ex} = 290 nm; λ_{em} = 325 nm).

This is much less marked in biotinylated AuNC 4a (Fig. S4e), for which the relative intensities match those of as-synthesised clusters. Remarkably, all indole AuNCi show absolutely no spectral nor intensity change upon thiopegylation and transfer into water

.

5. Au cluster size calculated from the Jellium model

The fluorescence intensity 2D maps shown in Figure 1 display high intensity spots that are associated with AuNCs. The emission wavelength of the maximal intensity, λ_{em}^{max}, as well the extremal wavelengths corresponding to 80% of this maximum are shown for both aniline and indole AuNCs in the first column of Table S5. The second column converts λ_{em}^{max} in energy units.

In the last column, the Jellium model is used to estimate, with an interval, the number of Au atoms of an AuNCs emitting at λ_{em}^{max} (E_f is the Fermi energy of bulk gold).

Type de Clusters	λ_{em}^{max} (80% range) (nm)	E (eV)	$n = \left(\dfrac{E_f}{E}\right)^3$
Indole	400 (375-430)	3,10	5 (4-7)
	425 (400-450)	2,92	7 (5-8)
Aniline	410 (350-450)	3,02	6 (4-8)
	500 (460-540)	2,48	11 (8-13)
	640 (600-670)	1,94	22 (18-26)

Table S5: AuNC size estimated from the fluorescence 2D maps using the Jellium model for both aniline and indole samples.

6. XPS analysis of functionalized AuNC
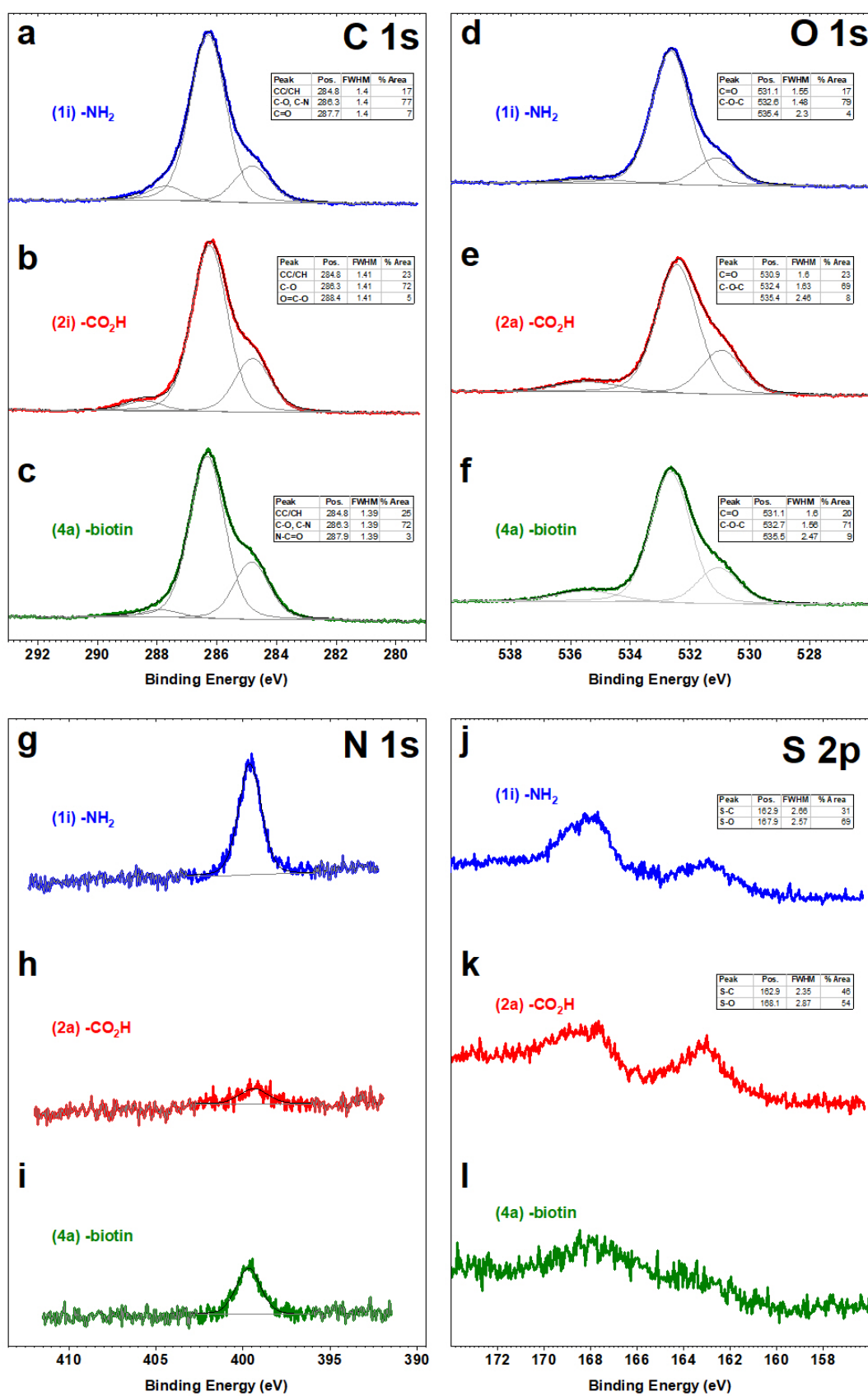
Figure S6: XPS spectra of –NH₂ (blue), -CO₂H (red) and –biotin (green) thiopegylated AuNC. (a-c) C1s level. (d-f) O1s level. (g-i) N1s level. (j-l) S2p level.

7. ElectroSpray Ionization Mass Specrometry of thiopegylated AuNCs

ESI-MS spectra of AuNC with PEG$_{12}$ containing ligands.

Figure 3, in the main text, presents the negative mode mass-to-charge ESI-MS spectra for (2a) and (2i) AuNCs exchanged with HS-PEG$_{12}$-COOH.

Three different cores from aniline-reduced clusters (2a) have been identified consistently with photophysical and XPS data: Au$_4$, Au$_7$ and Au$_{10}$. The dominant peaks numbered from 1 to 7 were associated with: , (**1**, m/z = 2906) [**Au$_7$**(S-PEG$_{12}$-CO$_2$H)$_7$]$^{2-}$, (**2**, m/z = 3222) [**Au$_7$**(S-PEG$_{12}$-CO$_2$H)$_8$]$^{2-}$, (**3**, m/z = 4154) [**Au$_{10}$**(S-PEG$_{12}$-CO$_2$H)$_{10}$]$^{2-}$.

Polymerized PEG$_{12}$-CO$_2$H fragments are also observed: (i) trimer (m/z = 1902), (ii) tetramer (m/z = 2535), (iii) pentamer (m/z = 3169)

Similarly, for indole-reduced clusters (2i), the dominant peaks, numbered from 1 to 8, suggest the presence of Au$_{10}$, Au$_{11}$ and Au$_{12}$ clusters: (**1**, m/z = 4168) [**Au$_{10}$**(S-PEG$_{12}$-CO$_2$H)$_{10}$]$^{2-}$, (**2**, m/z = 4471) [**Au$_{10}$**(S-PEG$_{12}$-CO$_2$H)$_{11}$]$^{2-}$, (**3**, m/z = 4569) [**Au$_{11}$**(S-PEG$_{12}$-CO$_2$H)$_{11}$]$^{2-}$, (**4**, m/z = 4788) [**Au$_{10}$**(S-PEG$_{12}$-CO$_2$H)$_{12}$]$^{2-}$,(**5**, m/z = 4885) [**Au$_{11}$**(S-PEG$_{12}$-CO$_2$H)$_{12}$]$^{2-}$, (**6**, m/z = 4984) [**Au$_{12}$**(S-PEG$_{12}$-CO$_2$H)$_{12}$]$^{2-}$, (**7**, m/z = 5304) [**Au$_{12}$**(S-PEG$_{12}$-CO$_2$H)$_{13}$]$^{2-}$, (**8**, m/z = 5619) [**Au$_{12}$**(S-PEG$_{12}$-CO$_2$H)$_{14}$]$^{2-}$

Figure S7 below provides a comparison between simulation and negative mode mass-to-charge ESI-MS spectra for each proposed molecular formula labeled as number (1-3) and (1-8) in Figure 3.
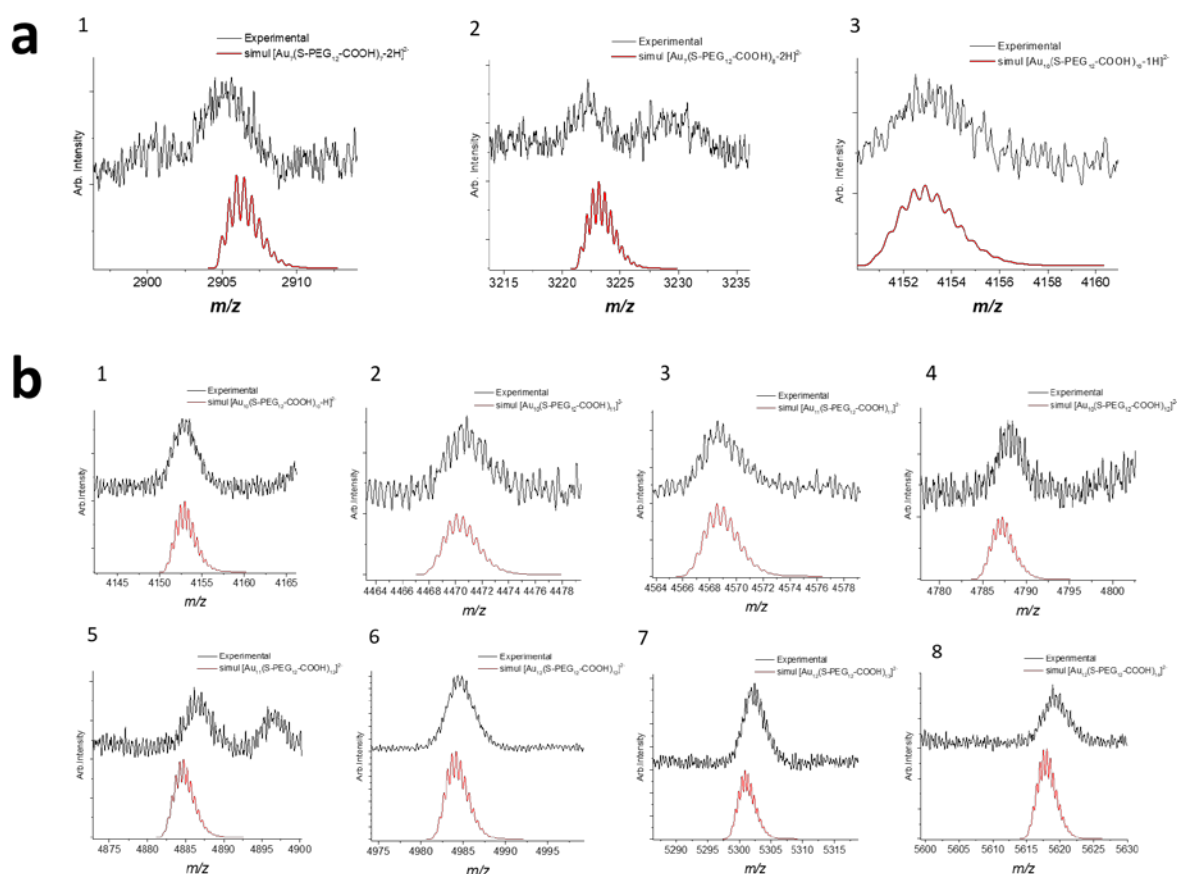
Figure S7. Comparison of simulation and negative mode mass-to-charge ESI-MS spectra for (a) aniline and (b) indole AuNCs respectively exchanged with HS-PEG$_{12}$-COOH from Fig 3a and 3b respectively. Panels are labelled according to the peak labels 1-3 and 1-8 in Figure 3.

The positive mode spectra of amine-stabilized AuNC shown in Figure S8 comprise a significant contribution of the PEG fragments, in particular in the $500 < m/z < 1500$ region, therefore preventing to assert the presence of very small AuNC. Yet, in the 1500-4000 region, one can observe peaks that can be matched to $Au_{25}(S-PEG_{12}-NH_2)_{19}$ with average mass of 16.4 kDa in (1a) and to $Au_{10}(S-PEG_{12}-NH_2)_{10}$ with average mass 8 kDa, plus $Au_8(S-PEG_{12}-NH_2)_8$ with average mass of 6.4 kDa in (1i).
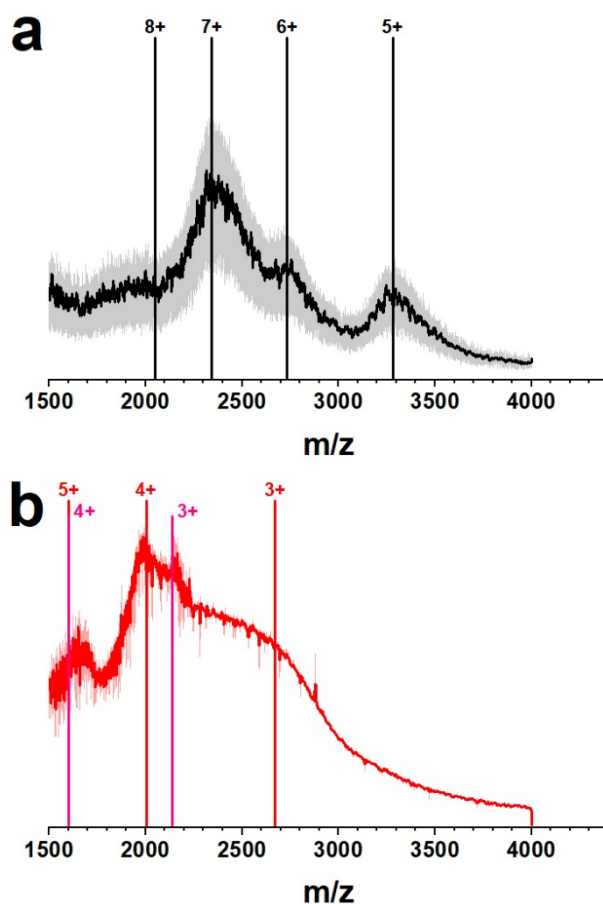
Figure S8: Positive mode mass-to-charge ESI-MS spectra for (1a) and (1i) AuNCs respectively exchanged with HS-PEG$_{12}$-NH$_2$ from aniline (panel a) and indole (panel b) gold clusters. A broad distribution of charge states is observed in both cases that can be assigned to $Au_{25}(S-PEG_{12}-NH_2)_{19}$ in (1a), as shown by the 5+ to 8+ markers in panel a, and to $Au_{10}(S-PEG_{12}-NH_2)_{10}$ with $Au_8(S-PEG_{12}-NH_2)_8$ in (1i) as indicated by the 3+ to 5+ red markers and 3+ to 4+ pink markers respectively in panel b. In both panels, smoothed data are shown in dark color on top of the fainted raw data.

ESI-MS spectra of AuNC with PEG$_{70}$ containing ligands.
The biotinylated AuNC 4a/4i were functionalized with a high molecular weight PEG spacer (~3 000 Da) in order to ensure their long term stability in aqueous solution. Figure S9 below shows the ESI-MS spectra in positive mode and its deconvolution using a multiplicative correlation algorithm.
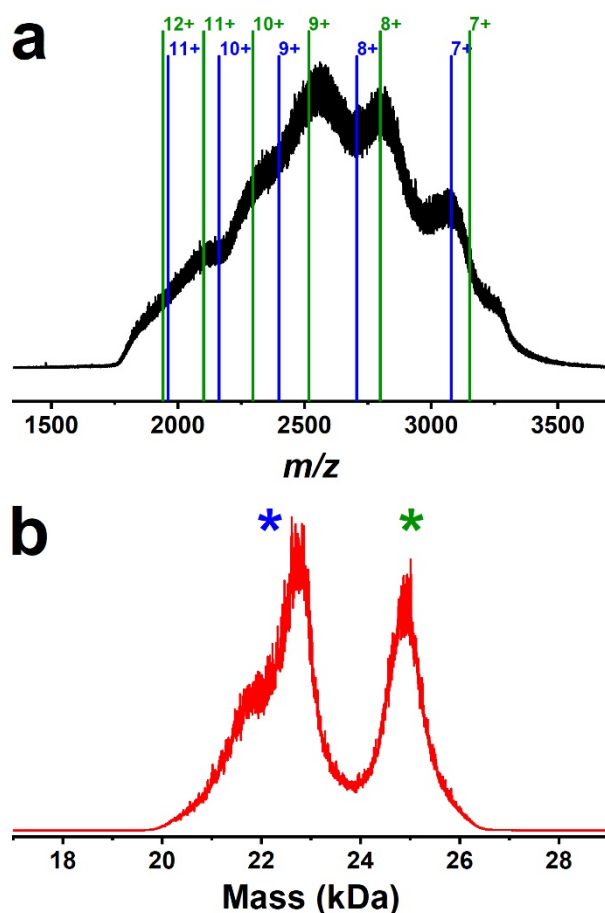
Figure S9: (a) Mass-to-charge spectra of 4a AuNCs stabilized with long biotinylated thioPEG ligands recorded in positive mode. Charge states for $Au_6(S\text{-}PEG_{70}\text{-}Biotin)_6$ and $Au_7(S\text{-}PEG_{70}\text{-}Biotin)_7$ are shown in blue and green lines respectively. (b) ESI-MS spectrum deconvoluted with a multiplicative correlation algorithm and showing two peaks compatible with Au_6 (blue marker) and Au_7 (green marker) AuNCs.

Note on MALDI-MS measurements

We also made attempts to measure the mass of the as-prepared Au NCs. For this purpose, we performed MALDI-MS measurements using a Voyager-DE PRO Biospectrometry Workstation from Applied Biosystems. A pulsed nitrogen laser of 337 nm was used for ionizing the sample, and alpha-Cyano-4-hydroxycinnamic acid was used as the matrix. The MALDI-MS show no information regarding intact nanoclusters. Only fragments or PEG envelopes were measured by MALDI-MS (data not shown).

8. HRTEM study of AuNCs

The direct size, morphology and structure characterization of sub-3 nm AuNCs remains challenging. Besides electrospray mass spectrometry (ESI-MS) and X-ray photoelectrons spectroscopy (XPS), the pristine AuNCs are characterized by high-resolution transmission electron microscope (HRTEM) as shown in Figures S10 and S11.

HRTEM images of non-thiolated AuNCs show no sign of aggregation, a homogeneous shape and a lognormal size distribution with an overall mean and standard deviation of the gold core diameter of 2.9 ± 1.6 nm and 2.4 ± 0.7 nm for aniline and indole reduced clusters respectively (Figs. S10a and S10b). These distributions underestimate the smallest clusters that have an extremely weak TEM contrast since the most stable form of AuNC with less than 13 atoms is considered to be flat oligomeric structures.[1–3] This suggests the coexistence of clusters with different optical properties. Clusters with diameters larger than 2.2 nm are considered poor emitters while clusters smaller than 2.2 nm exhibit linear and non-linear luminescence[4]. Since our samples precisely overlap this boundary, as confirmed by atomic force microscopy measurements yielding a height of 1.7 ± 0.7 nm (ESI Fig. S12), we have further examined the AuNCs morphology. Essentially, four different structures of AuNCs are observed in both aniline- and indole-reduced samples and show a gradual shift in size distribution (Figs. S10c-f). A lattice parameter of 2.35 Å could be observed for all shapes, that corresponds to the (111) plane family of a gold face-centered cubic crystal packing (See also Fig. S11).
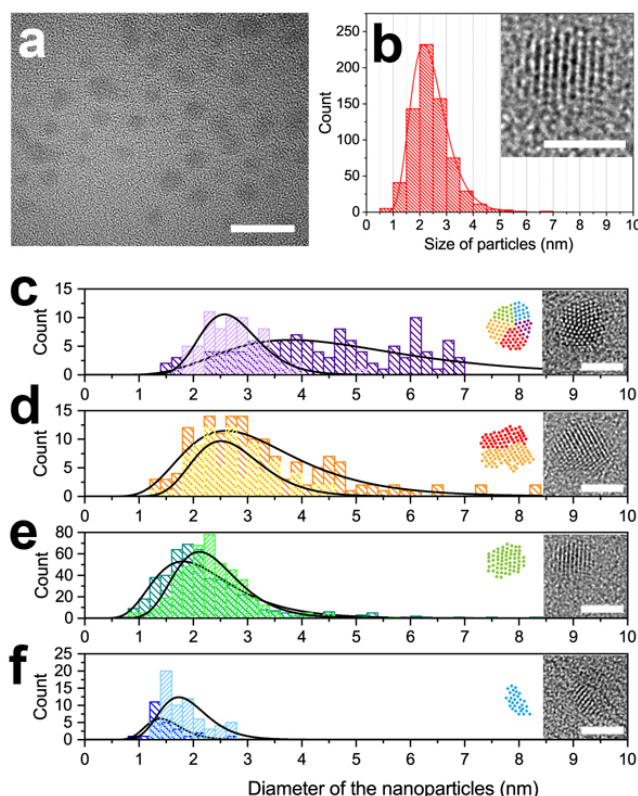
Figure S10. (a)Typical HRTEM image of as-synthesized indole AuNCs. (b) Size distribution of the indole AuNCs. The mean size is 2.4 ± 0.7 nm. Inset: close-up TEM image displaying the crystal lattice of one indole AuNC. (c-f) Size histograms of indole (lighter colors) and aniline (darker colors) AuNCs sorted into shape classes illustrated by the TEM image and colored sketch insets: (c) pentatwin, (d) single twin, (e) isotropic single crystal, (f) oblong single crystals. Scale bars 2 nm. Black lines are lognormal fits.

The larger AuNCs (5.0 ± 2.2 nm with aniline and 2.7 ± 0.6 nm with indole) are composed of 5 twins but represent only 14-16%. The second larger structures (3.3 ± 1.3 nm with aniline and 2.7 ± 0.7 nm with indole) are single twinned and amount to 11-20%. The two smallest sub-populations appear single crystalline but present two different shapes. The isotropic structures represent 61-66% (2.27 ± 0.91 nm with aniline and 2.36 ± 0.65 nm with indole). The oblong AuNCs amounts to 3-9% and their longer and

shorter axes are 1.51 ± 0.35 nm and 1.07 ± 0.11 nm with aniline and 1.90 ± 0.47 nm and 1.04 ± 0.16 nm with indole respectively. These smallest and lower contrast nanostructures could be commensurate with Au10 to Au13 that sit at the onset between 2D and 3D morphologies, have a typical size of ca. 1.1-1.2 nm and show oblong anisotropy in the more stable 2D forms[2,3].
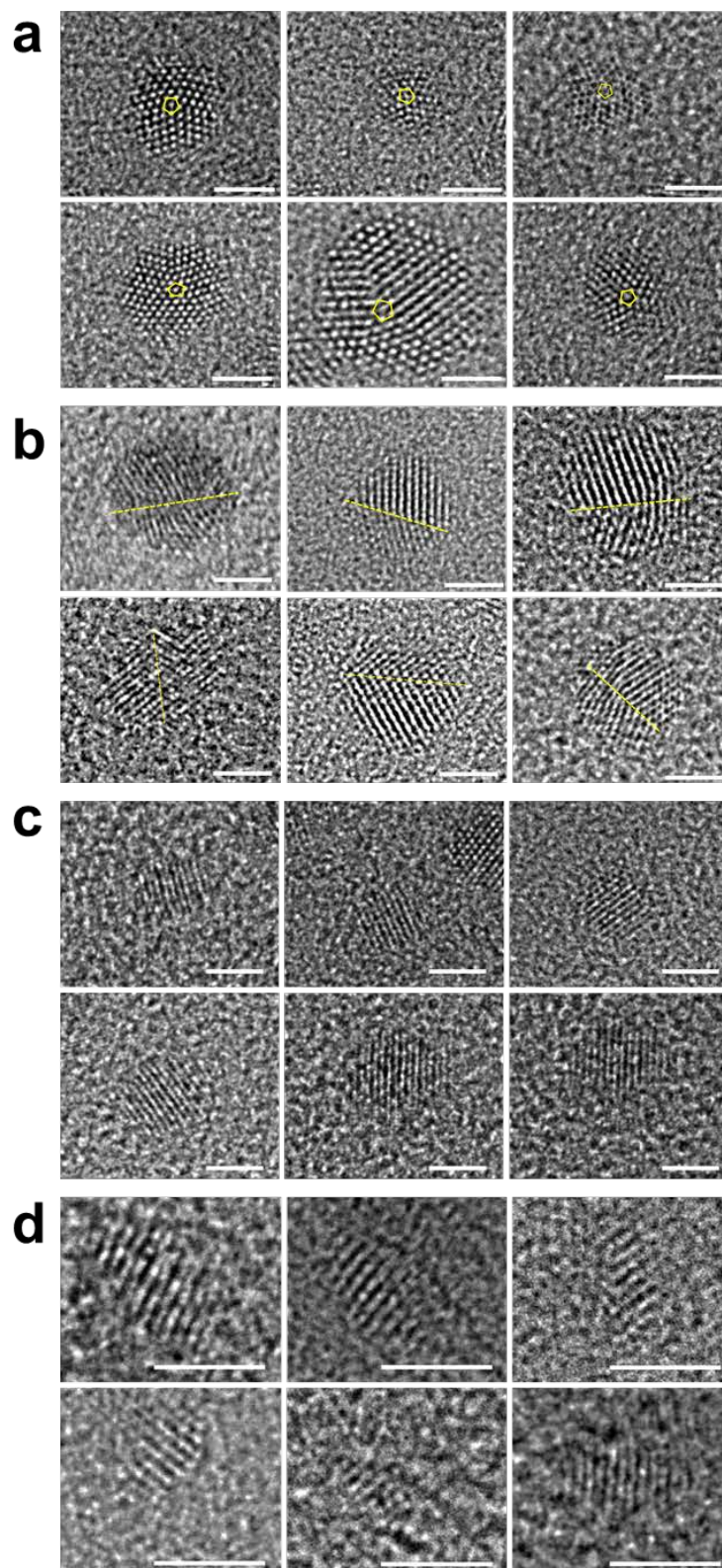
Figure S11: High resolution TEM micrographs of as-synthesized (a) pentatwinned, (b) single twinned, (c) isotropic single crystalline and (d) oblong single crystalline AuNCs. Scale bars are 2 nm.

9. AFM topography of AuNCs

The AuNCs were dispersed on a freshly cleaved mica substrate by drop-casting and drying a microdroplet. AFM images were acquired on a Brucker DI 3000 microscope operated in intermittent mode using OTESPA silicon tips (Bruker, ca. 300 kHz resonance). A typical AFM image of AuNCs is shown in Fig. S3a and is compared with an image of a pristine mica surface in Fig. S3 b. Height profiles and height histograms of both samples are plotted in Figures S3 c,d and S3e,f respectively.

The clear presence of dispersed dots with lateral size of ca. 20 nm limited by the tip convolution and height of a few Angstroms is consistent with the TEM images and the size histograms shown in Fig. S9 and can be ascribed to AuNCs. If one considers the AFM height as the relevant size gauge the AuNC apparent size, the average height is 1.7 nm ± 0.7 nm. This suggests the presence of sub-3 nm clusters.
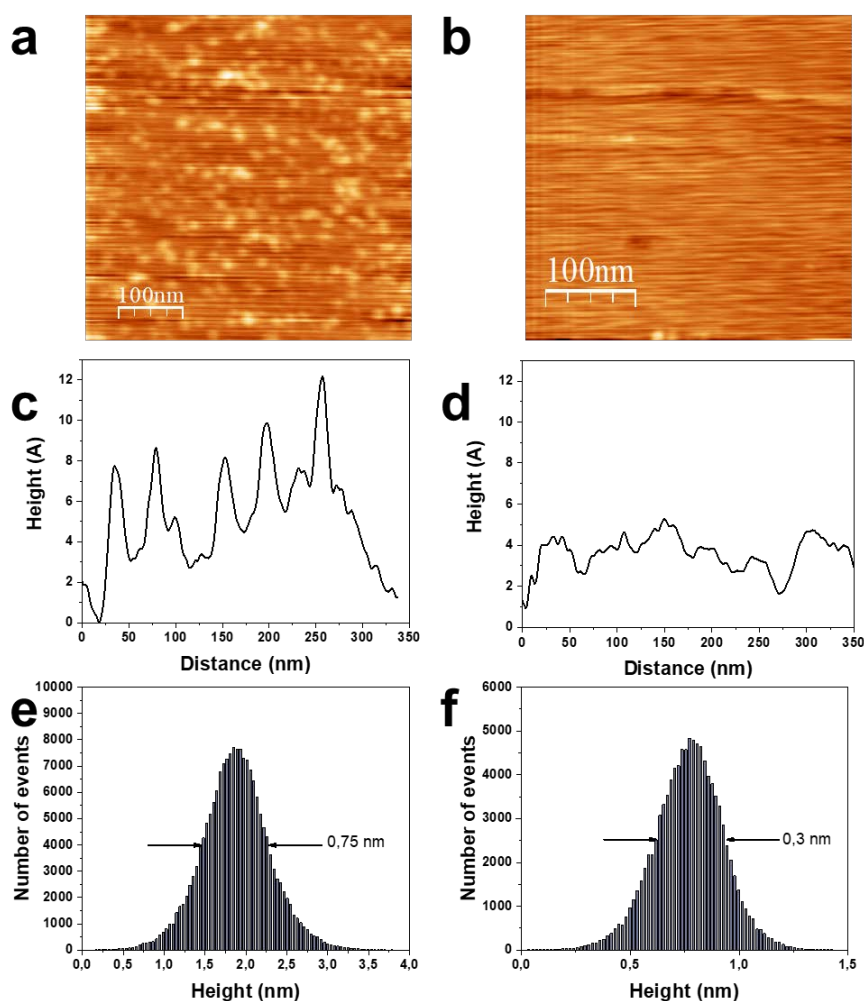
Figure S12: (a-b) AFM topography images of AuNCs on mica and freshly cleaved mica. (c-d) Height profiles of the surface of AuNCs on mica and mica alone. (e-f) Histograms of the height of the samples: 1.7 nm ± 0.7 nm for AuNCs on mica and 0.7 nm ± 0.3 nm on cleaved mica.

10. Fluorescence lifetime fitting procedure and measurements of thiopegylated AuNCs

Our deconvolution procedure consists in considering an increasing number of exponential functions, performing the fit, calculating residues and their χ^2 values. We observe that χ^2 reaches a minimal plateau as more recombination times are considered (Fig. S13). The selected configuration corresponds to the minimal χ^2 with the least number of exponentials and are highlighted by the colored rectangle in Fig. S13. Out of two (for AuNC$_i$) or three (for AuNC$_a$) recombination times, the shortest lifetime was ca. 0.5 ns in all cases. However, our setup records a 50 ns time window over 1024 channels, i. e. 0.049 ns per channel. The resulting experimental time resolution makes it difficult to assert lifetimes shorter than 1 ns. Therefore, we ignored the shortest values obtained from the fits and consider a mono and bi-exponential decay for AuNC$_i$ and AuNC$_a$ respectively.

Note that in our deconvolution routine, the POPOP response (grey in Fig. 4 and S14) is fitted with a single exponential, deconvoluted into an experimental IRF that is then convoluted with 1, 2, 3 or 4 exponentials to be fitted to the fluorescence decay data of the clusters solutions. The inferred IRF is not plotted in the fitting process.
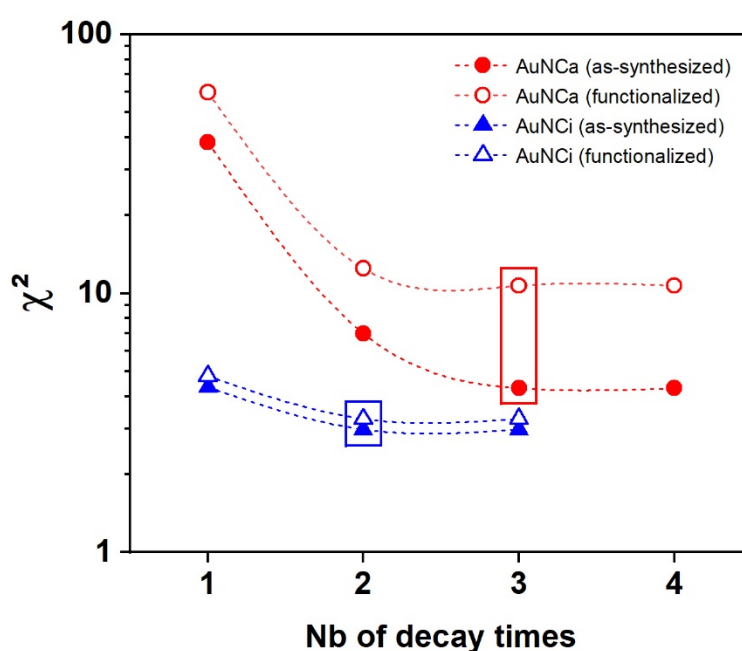
Figure S13. Evolution of the χ^2 values of the fluorescence lifetime fits with the number of different decay times considered for the aniline (red) and indole (blue) gold clusters. Boxes highlight the selected models.

The fluorescence lifetime measurements for biotin-functionalized aniline (4a) and indole (4i) AuNC shown in Figure S14 do not show any difference with the data for as-synthesized AuNC shown in Figure 4. The lifetime for aniline AuNC 4a is fitted with two decreasing exponentials at 4.0 ± 0.01 ns (90%), and 76.9 ± 0.5 ns (10%). The lifetime of indole AuNC 4i is fitted with one exponential at 8.2 ± 0.1 ns. The exactly matching fit parameters further confirms that the introduction of thiopegylated ligand has virtually no effect on the photophysical properties of the AuNC. It strongly suggests that the HS-PEG$_n$-R ligand exchange does not affect the emitting center structure and immediate environment.
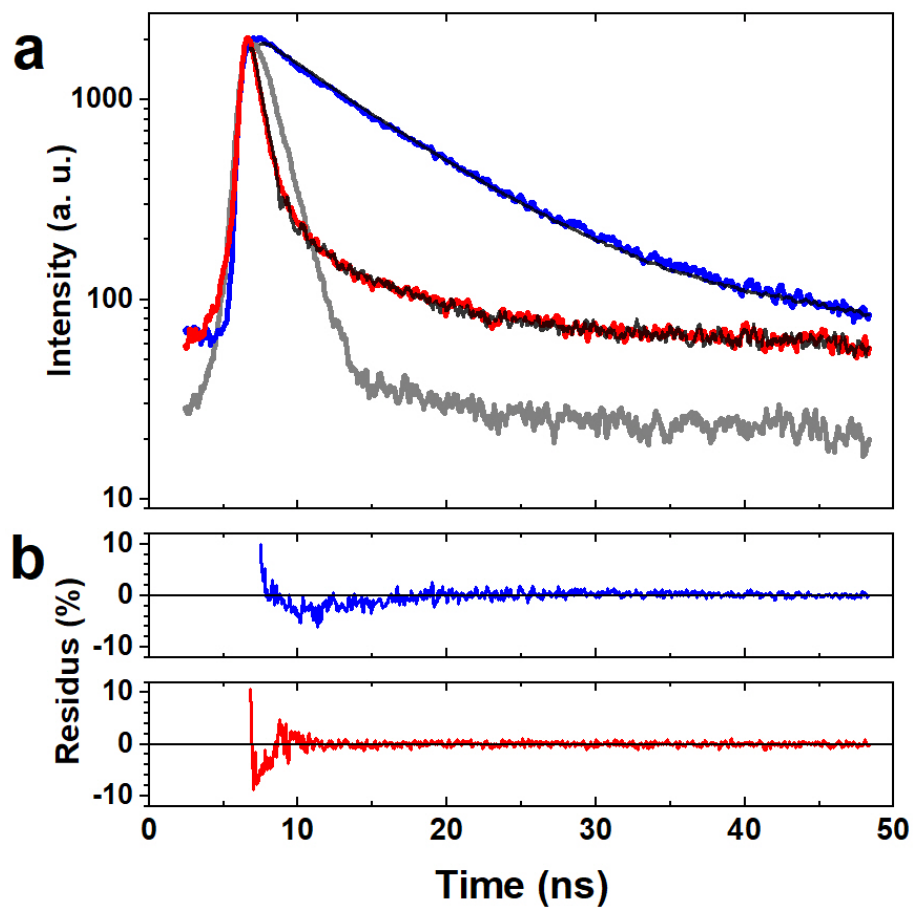
Figure S14. (a) Fluorescence lifetime measurements and (b) fit residues of biotin-functionalized aniline (4a, red) and indole (4i, blue) AuNCs. In (a), fits are in black and the POPOP reference used is in grey.

11. Analysis of quantum yields reported in the literature for water-soluble AuNC

Figure S15 gathers quantum yields of AuNC in water, as reported in the literature by many groups, as a function of the cluster size. This size is either known from available MS experiments or DFT modelization (blue squares) or inferred from available fluorescence spectra using the Jellium model (black squares). Two distinct trends are observed as clearly pointed out by the shaded zones.

Grey zone: AuNC stabilized with small molecular ligands tend to show quantum yield around 5-10% irrespective of their size between 5 and 40 Au atoms.[5–15]

Blue zone: Au NC stabilized by large or polymeric ligands such as PAMAM dendrimers,[16,17] PEG_n with n=550 or 750,[11] cellulose[18], or polyallylamine hydrochloride[19,20] show a higher quantum yield (10-15%) that drastically increases up to 70% as the AuNC size decreases down to 5 atoms.

The reason invoked for this marked increase of the quantum yield is the presence of a thick or rigid shell around the fluorescent gold core that stiffens the gold shell surface and alters directly the luminescence of the triplet state.[21]
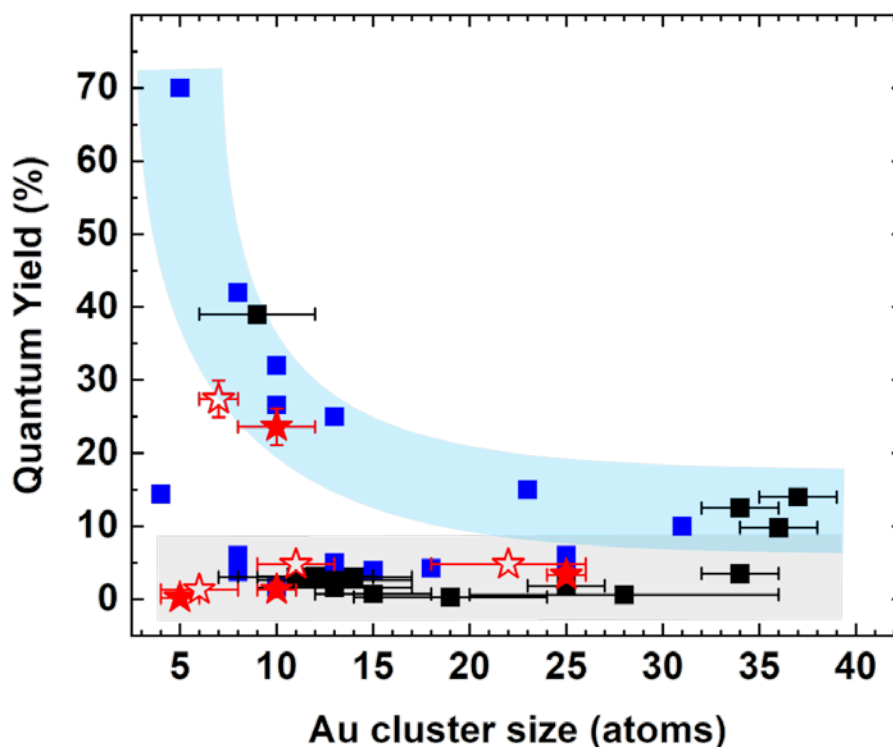
Figure S15. Quantum yields of AuNC reported in the literature (black and blue squares) as a function of cluster size as measured by MS or fixed in DFT models (blue squares) or inferred from luminescence spectra by the Jellium model (black squares). Data reported in this work are inserted as red stars with full symbols when the size is determined by MS (for functionalized AuNC in water) and empty symbols when it is inferred from the Jellium model (for as-synthesized AuNC in EG). Blue and grey shaded zones are only guides for the eye.

When the data reported in this work are added to Figure S15 (red stars), one observes that the green and red emitting AuNC fit into the grey zone as most clusters stabilized with small ligands while the violet/blue emitting AuNC that exhibit a 27% quantum yield reach the blue zone even though the ligand used are much smaller (the larger ones have a PEG_{70} spacer). Note that empty red stars correspond to as-synthesized AuNC in ethylene glycol while full red stars indicate functionalized AuNC in water as the literature data.

12. Quantum yield of thiopegylated AuNC

AuNC type	λex (nm)	QY (in EG)		AuNC type	QY (in H_2O)
AuNCa	317	1.3% ± 0.5%		4a	0.2% ± 0.5%
AuNCa	395	4.8% ± 0.5%		4a	1.3% ± 1.0%
AuNCa	530	4.8% ± 0.5%		4a	3.3% ± 1.0%
AuNCi	317	27.4% ± 2.5%		4i	23.6% ± 2.5%

Table S16: Quantum yield (QY) values measured for as-synthesized AuNC$_a$ and AuNC$_i$ clusters in ethylene glycol and for thiopegylated AuNC 4a and 4i in water.

13. References

1 A. Soleilhac, F. Bertorelle, C. Comby-Zerbino, F. Chirot, N. Calin, P. Dugourd and R. Antoine, *J. Phys. Chem. C*, 2017, **121**, 27733–27740.
2 M. P. Johansson, A. Lechtken, D. Schooss, M. M. Kappes and F. Furche, *Phys. Rev. A*, 2008, **77**, 053202.
3 M. P. Johansson, I. Warnke, A. Le and F. Furche, *J. Phys. Chem. C*, 2014, **118**, 29370–29377.
4 S. H. Yau, O. Varnavski and T. Goodson, *Acc. Chem. Res.*, 2013, **46**, 1506–1516.
5 J. Xie, Y. Zheng and J. Y. Ying, *J. Am. Chem. Soc.*, 2009, **131**, 888–889.
6 C.-A. J. Lin, T.-Y. Yang, C.-H. Lee, S. H. Huang, R. A. Sperling, M. Zanella, J. K. Li, J.-L. Shen, H.-H. Wang, H.-I. Yeh, W. J. Parak and W. H. Chang, *ACS Nano*, 2009, **3**, 395–401.
7 Y. Bao, H.-C. Yeh, C. Zhong, S. A. Ivanov, J. K. Sharma, M. L. Neidig, D. M. Vu, A. P. Shreve, R. B. Dyer, J. H. Werner and J. S. Martinez, *J. Phys. Chem. C*, 2010, **114**, 15879–15882.
8 X. Le Guével, B. Hötzer, G. Jung, K. Hollemeyer, V. Trouillet and M. Schneider, *J. Phys. Chem. C*, 2011, **115**, 10955–10963.
9 L. Shang, N. Azadfar, F. Stockmar, W. Send, V. Trouillet, M. Bruns, D. Gerthsen and G. U. Nienhaus, *Small*, 2011, **7**, 2614–2620.
10 H. Kawasaki, K. Hamaguchi, I. Osaka and R. Arakawa, *Adv. Funct. Mater.*, 2011, **21**, 3508–3515.
11 F. Aldeek, M. A. H. Muhammed, G. Palui, N. Zhan and H. Mattoussi, *ACS Nano*, 2013, **7**, 2509–2521.
12 K. G. Stamplecoskie and P. V. Kamat, *J. Am. Chem. Soc.*, 2014, **136**, 11093–11099.
13 P.-C. Chen, A. P. Periasamy, S. G. Harroun, W.-P. Wu and H.-T. Chang, *Coord. Chem. Rev.*, 2016, **320–321**, 129–138.
14 S. Zhou, Y. Duan, F. Wang and C. Wang, *Nanoscale*, 2017, **9**, 4981–4988.
15 X. Jiang, X. Wang, C. Yao, S. Zhu, L. Liu, R. Liu and L. Li, *J. Phys. Chem. Lett.*, 2019, **10**, 5237–5243.
16 J. Zheng, J. T. Petty and R. M. Dickson, *J. Am. Chem. Soc.*, 2003, **125**, 7780–7781.
17 J. Zheng, C. Zhang and R. M. Dickson, *Phys. Rev. Lett.*, 2004, **93**, 077402.
18 S. K. Kailasa, M. R. Kateshiya and N. I. Malek, *J. Mol. Liq.*, 2020, **319**, 114305.
19 M.-M. Xu, T.-T. Jia, B. Li, W. Ma, X. Chen, X. Zhao and S.-Q. Zang, *Chem. Commun.*, 2020, **56**, 8766–8769.
20 T.-T. Jia, B.-J. Li, G. Yang, Y. Hua, J.-Q. Liu, W. Ma, S.-Q. Zang, X. Chen and X. Zhao, *Nano Today*, 2021, **39**, 101222.
21 K. Pyo, V. D. Thanthirige, K. Kwak, P. Pandurangan, G. Ramakrishna and D. Lee, *J. Am. Chem. Soc.*, 2015, **137**, 8244–8250.